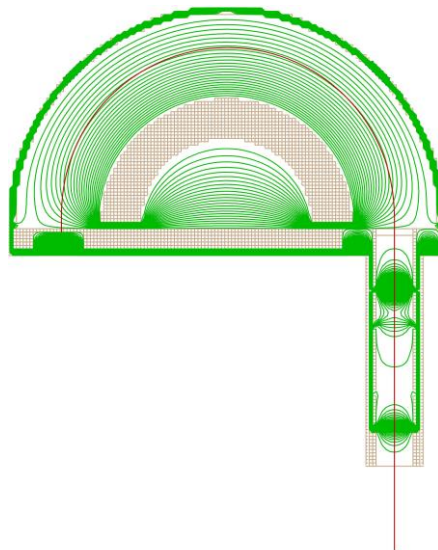




**UNIVERSITY OF CRETE**

**DEPARTMENT OF PHYSICS**

Experimental Energy Resolution of a Paracentric  
Hemispherical Deflector Analyzer for Different  
Entry Positions and Bias



Gennarakis Giannis

*Supervisor: Prof. Theo J. M. Zouros, Univ. of Crete*

*Heraklion, 2015*

**May 2015**

# **Dissertation**

## **Experimental Energy Resolution of a Paracentric Hemispherical Deflector Analyzer for Different Entry Positions and Bias**

**Gennarakis Giannis**

**Supervisor:**

Prof. Theo J. M. Zouros, *Univ. of Crete*

## Abstract

Results from the simulation of a biased paracentric hemispherical deflector analyzer (HDA) with injection lens are presented. The finite differences electron optics software SIMION was used to perform Monte Carlo type trajectory simulations in an effort to investigate the focusing effects of the HDA entry and exit fringing fields which are used to improve energy resolution - a novel feature of this type of analyzer. Comparisons to recent experimental results are also presented. Biased paracentric HDAs represent a novel class of HDAs, which use the lensing action of the strong fringing fields at the HDA entry, to restore the first order focus characteristics of ideal HDAs in a controlled way. The improvement in energy resolution and transmission without the use of any additional fringing field correction electrodes is of particular interest to modern analyzers using position sensitive detectors.

SUBJECT AREA: Electron spectroscopy, Ion-Atom collisions, Atomic Physics

KEYWORDS: *Hemispherical Analyser, SIMION, Electron Spectroscopy, Electrostatic lens*

## Acknowledgments

Being involved in scientific research for the first time of my life, I would specially like to thank Prof. Zouros for giving me this ability, and making this small but worthwhile journey smooth, through his patience with new students, clear scientific thought and all the things that taught me on how to do the research and think. Also, for the spirit of teamwork that he promoted to all the members of the research and his unlimited time to keep the project going. Furthermore, I would like to thank Prof. Genoveva Martinez Lopez for her comments and advice on various matters concerning the simulation method and results, as well as Dr. Omer Sise for giving us his lights on how to exploit the old data and overtake obstacles during the experimental process and results. Last but not least, the creator of software SIMION, Mr. David Manura for all the debugging and coding tips that kept us moving forward till the end.

### Special acknowledgment to the funding source

This research has been co-financed by the European Union (European Social Fund ESF) and Greek national funds through the Operational Program "Education and Lifelong Learning" of the National Strategic Reference Framework (NSRF) Research Funding Program: THALES. Investing in knowledge society through the European Social Fund, grant number MIS 377289).

## Nomenclature

| Symbol                    | Units | Description   |
|---------------------------|-------|---|
| $D_\gamma$                | (mm)  | $\gamma$ -independent dispersion length                                       |
| $E_{s0}$                  | (eV)  | Nominal electron gun energy   |
| $R_0 = \bar{R}$           | (mm)  | HDA mean radius   |
| $R_B = \Delta E_B/E$      | (-)   | HDA Base Energy Resolution  |
| $R_\pi$                   | (mm)  | Radius of exit of the beam  |
| $V_0$                     | (V)   | Nominal voltage $V(R_0)$  |
| $V_1$                     | (V)   | Nominal voltage $V(R_1)$ on $R_1$   |
| $V_2$                     | (V)   | Nominal voltage $V(R_2)$ on $R_2$   |
| $V_p$                     | (V)   | Nominal voltage on the HDA front plate  |
| $E_0$                     | (eV)  | Nominal electron HDA pass energy  |
| $F$                       | (-)   | Pre-retardation ratio $-E_{s0}/E_0$   |
| $M$                       | (-)   | HDA linear magnification  |
| $T$                       | (eV)  | Initial kinetic energy of the particle  |
| $V(r)$                    | (V)   | HDA potential, $V(r) = -k/r + c + V_p$  |
| $W$                       |       | Undecelerated tuning energy   |
| $w$                       | (eV)  | Energy of the central trajectory or tuning energy (after deceleration)        |
| $\Delta E_B = FBM$        | (eV)  | Base energy resolution; full width of the energy transmission function.       |
| $\Delta E_p$              | (eV)  | Individual particle energy relative to the pass energy of the analyzer.       |
| $\Delta R = R_2 - R_1$    | (mm)  | Distance between the hemisphere plates  |
| $\Delta R_\pi$            | (mm)  | Exit beam width along the energy dispersion direction                         |
| $\Delta E = FWHM$         | (eV)  | Full width at half of the maximum height of the energy transmission function. |
| $\alpha$                  | (deg) | Angle of particle prior to entering the HDA                                   |
| $\gamma$                  | (-)   | Control Parameter to set $V_0$  |
| $\xi$                     | (-)   | HDA parameter $\xi = R_\pi/R_0$   |
| $\rho = \Delta R/\bar{R}$ | (-)   | Interradial separation  |
| $\tau = t/w$              | (-)   | Reduced pass energy   |

## Contents

|   |    |
|---|----|
| Introduction.....   | 7  |
| Historical Review .....                                       | 7  |
| Electron Spectroscopy .....                                   | 8  |
| Photoelectron Spectroscopy (PES) .....                        | 8  |
| Auger Spectroscopy .....                                      | 8  |
| Zero Degree Auger Projectile Spectroscopy.....                | 9  |
| Electrostatic Analysers .....                                 | 9  |
| Theory.....   | 10 |
| Motion of a charged particle in an ideal $1/r$ potential..... | 11 |
| Derivation of a charged particle trajectory .....             | 13 |
| Focusing Conditions of the Ideal HDA.....                     | 14 |
| Spectrograph basic equation.....                              | 15 |
| Analyzer Voltages .....                                       | 15 |
| Ion Optics Simulation Software SIMION.....                    | 17 |
| References.....   | 18 |
| Appendix A (Works Cited) .....                                | 19 |
| Appendix B (Research Papers Published).....                   | 20 |

## Introduction

Electron energy analyzers which are a vital component of electron spectrometers have become important tools in many branches of collision physics. In order to resolve higher electronic states and vibrational states in these experiments, some sort of electron energy analyzer is required to provide an incident beam of sufficiently narrow energy spread and to determine the energy of the scattered or ejected electrons. The most common arrangement is to use a hemispherical deflector analyzer.

## Historical Review

The history of electron spectroscopy goes back more than 100 years when first H. Hertz reported in 1887 [1] about the matter-light interaction famously known as “the photoelectric effect” which was later described extensively by A. Einstein in 1905 [2]. Two years after Einstein's publication, in 1907 P. D. Innes experimented with a Röntgen tube, Helmholtz coils, a magnetic field hemisphere (an electron momentum analyzer), and photographic plates to record broad bands of emitted electrons as a function of velocity, in effect recording the first X-Ray Photoelectron Spectroscopy (XPS) spectrum [3]. The “scattering experiment”, initiated in 1911 by Rutherford in his famous experiment of bombarding thin gold films with  $\alpha$ -particles [4], provided valuable information both on the structure and on the interaction potential of the partners involved. The fundamental aspects of atomic collision theory were already formulated by Mott and Massey in their monumental work first published in 1933 [5]. However, interest remained focused solely on nuclear physics for the next 30 years.

It wasn't until the early 1960's when the tandem Van de Graaff ion accelerators, popular in nuclear physics by the time, were implemented in atomic physics, primarily due to the fact that projectile-ions can excite atomic states inaccessible by photon and electron impact. Shortly, the use of light ions, available in most of the charge states and in a wide band of collision energies, became a unique tool in atomic physics studies. At the same time, the increasing interest in the investigation of the Auger and auto-ionization effects made the use of electrostatic spectrometers wide spread.

Today, tandem Van de Graaff accelerators, Linear Accelerators, Electron Cyclotron Resonance (ECR) ion sources, Electron Beam Ion Sources (EBIS) and Storage Rings, can provide atomic ions from hydrogen to uranium in all charge states and in energies varying from a few eV/u to hundreds of MeV/u, depending on the atomic species, the charge state and the source in use. A large variety of energy dispersive spectrometers like the parallel plate analyser, the cylindrical plate analyser, the toroidal analyser, the hemispherical analyser and spherical plate analyser are also extremely popular, indicating the continuous interest in the physics of ion-atom collisions, as also the wide development of different experimental techniques, as for example the most modern COLd Target Recoil Ion Momentum Spectroscopy (COLTRIMS) experiments.

## Electron Spectroscopy

The term electron spectroscopy refers to methods where the sample is ionized and the emitted electrons are observed. The most common type is *photoelectron spectroscopy*, in particular X-ray photoelectron spectroscopy (XPS) but also the UV photoelectron spectroscopy (UPS) is widely used.

### Photoelectron Spectroscopy (PES)

Photoelectron spectroscopy (PES) is a method where the molecule is ionized by irradiating it with such photons that an electron is released. When using moderate photon energies in the far ultraviolet region, only the weakly bound valence electrons can be released while a harder rays in the X-ray region will also release electrons from the innermost core orbitals.

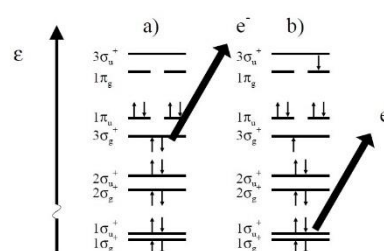


Fig. 1 (a) UPS; (b) XPS

When UV light is used the method is called *UV photoelectron spectroscopy (UPS)* and when X-rays are used it is called *X-ray photoelectron spectroscopy (XPS or ESCA (Electron Spectroscopy for Chemical Analysis))*. The principle of these methods are shown schematically in Fig. 1.

### Auger Spectroscopy

Ionization in one of the innermost core molecular orbitals results in a very highly excited ion. A number of spontaneous relaxation processes may ensue. In the *Auger process* the hole in the core orbital is filled by dropping down a valence electron. This creates a new hole in the valence shell. At the same time a large amount of energy is released because the energy of the core orbital is much lower than that of the donating valence orbital. This energy is used to release another valence electron. The principle of the process is shown schematically in Fig.2. A pure Auger spectrum is shown in Fig.3. It is a spectrum of lithium fluoride in gas phase.

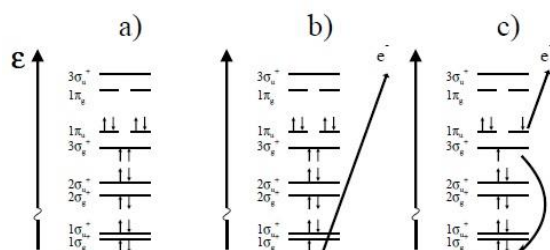


Fig. 2 Auger Spectroscopy:  
a) the ground state; b) ionization in X-ray photoelectron spectroscopy; c) the Auger process

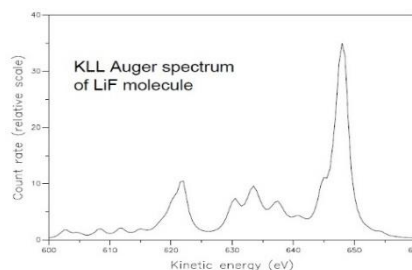


Fig. 3 The Auger spectrum of Lithium fluoride

The Auger process is customarily described by indicating in which shell the original ionization occurred and where the final two holes reside in the electronic structure of the doubly ionised molecule. In LiF the initial X-ray ionisation extracted an electron from the K shell. Afterwards the hole was filled by an electron from the L shell and finally one further electron was ejected from the L shell.

### Zero Degree Auger Projectile Spectroscopy

Projectile ions are mostly moving at relatively high velocities. Consequently, the Auger lines from projectile ions suffer considerable kinematic effects. A very popular method to improve the intrinsic analyser resolution, is to perform electron deceleration prior to their analysis in the spectrometer. However, the tremendous decrease of the electron transmission, present in all spectrographs utilizing slits, sets a practical limit on the applied deceleration and therefore to the achieved energy resolution. To improve the energy resolution the projectile Auger electrons are detected at  $0^\circ$  or  $180^\circ$  with respect to the beam direction, as in this way substantial reduction of the kinematic broadening can be achieved. The technique of detecting Auger electrons emitted from ions at  $0^\circ$  with respect to the beam direction, is known as *Zero-degree Auger Projectile Spectroscopy (ZAPS)* and has received considerable attention the past two decades. The potential advantage of this technique is that it is the only efficient method which can provide state-selective cross section information about collision mechanisms.

### Electrostatic Analysers

A CHA (Concentric Hemispherical Analyser), also known as an HDA (Hemispherical Deflector Analyser), consists of two metal hemispheres. They are arranged such that their centers of curvature are coincident as shown in Fig.4. Different voltages are placed on each hemisphere such that there is an electric field between the two hemispheres. Electrons are injected into the gap between the hemispheres. If the electrons are travelling very fast, they will impinge on the outer hemisphere. If they are travelling slowly, they will be attracted to the inner hemisphere. Hence only electrons in a narrow energy region (called the pass energy) succeed in getting all the way round the hemispheres to the detector. A series of lenses are placed before the HDA. The lenses enable two operating modes - Constant Retardation Ratio (CRR), or Constant Analysis Energy (CAE). With CRR mode, the electrons are slowed down by an amount which is a constant ratio of the electron energy to be analyzed (see also RFA - Retarding Field Analyser). For example, if the retardation ratio is 10, and 1000eV electrons are to be analysed, then the electrons will be slowed down to 100eV, and the pass energy will be set to 100 eV. In the CAE mode, the pass energy is fixed. Hence if the pass energy is 50 eV, then electrons of 1000eV will have to be slowed down by 950 eV in order to be detected. The CRR mode gives constant  $E/\Delta E$  resolving power and the CAE mode gives constant  $\Delta E$  energy resolution.

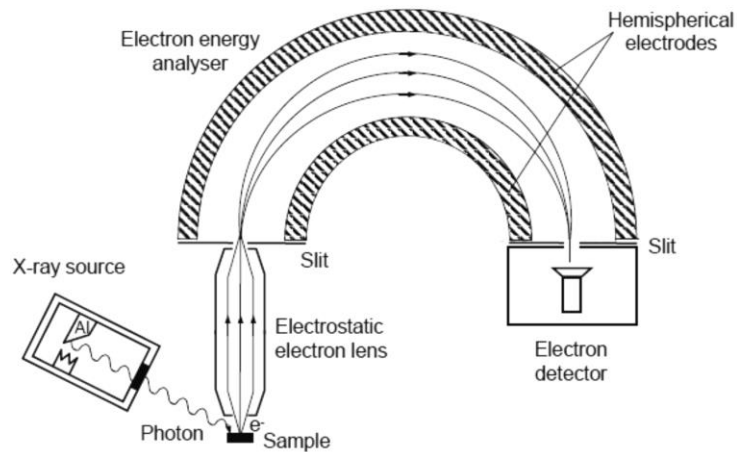


Fig. 4 Schematic of an HDA (or CHA) comprised of two concentric metal hemispheres with different voltages

## Theory

First Hughes and Rojansky [6] mentioned in their paper the possibility of energy analyzing charged particles using electrostatic fields instead of magnetic fields. It was already well known by that time (1929) that electrons entering with small angles in a cylindrical spectrograph with magnetic fields, describe a circle whose radius depends on the velocity of the electrons and the strength of the magnetic fields and that good refocusing happened at  $\varphi = 180^\circ$  from the plane containing the entrance slit. For electrostatic fields they found that positions  $180^\circ$  and  $90^\circ$  (of the plane of the receiving slit) were not suitable for good refocusing and instead suggested good re-focusing and good resolution to be found at a characteristic angle of  $\Phi = 127^\circ 17'$ .

A few years later Purcell [7] considered the refocusing properties of charged particles in an ideal (no fringing fields) spherical condenser and studied the possibility of deflecting and focusing a slightly diverging beam of charged particles in a cylindrical condenser. He described this device as an energy-analyser where the trajectory of a nonrelativistic particle in any given electrostatic field depends only on its initial position and direction and the ratio of its charge to its initial kinetic energy. These types of analysers were previously incorporated successfully as mass spectrographs. Ever since, the hemispherical version of the condenser became very popular in electron spectroscopy – due to its advantageous focusing properties and rugged construction – and many hemispherical spectrometers were studied and utilized in experiments.

In 1967 Kuyatt and Simpson developed [8] an electron monochromator design based on a hemispherical analyser. They examined the slit width and electron energy at a given resolution for obtaining maximum current. They concluded on the choice of equal size round apertures for the entrance and exit of the beam instead of slits with dimensions satisfying the equation  $\alpha^2 = w/2\bar{R}$  (where  $\alpha$  is the pencil angle,  $w$  the aperture diameter and  $\bar{R}$  the mean analyser radius) which became a standard criterion for HDA designs. Paolini and Theodoridis, and Kennedy et. al. reported on the transmission properties of spherical plate electrostatic analysers. Roy and Carette, included the hemispherical spectrometer in their method of calculating the energy distribution of electrons selected electrostatically. Heddle reported on

the comparison of the étendue (the product of the entrance area and solid angle) of electron spectrometers including spherical plate analysers. Polaschegg reported on the features of the spherical analysers with and without pre-retardation. He also reported on the study of the energy resolution and the intensity behavior of the spherical analysers as a function of the entrance parameters. Imhof et. al. studied the energy resolution and transit time spread in the hemispherical analysers involved in coincidence experiments. Kevan also reported on design criteria for high-resolution angle-resolving HDAs. Hadjarab and Erskine reported on the image properties of the HDA used with a position sensitive detector (PSD), replacing in this way the commonly used exit slit with a large area detector. A double-stage spectrograph consisting of two HDAs has been reported by Mann and Linder, as well as Baraldi and Dhanak. Page and Read investigated the energy non-linearity of HDA when used with a multi-detector anode or PSD.

In the previous references, the HDA was studied as if the electrostatic field was ideal, i.e. fringing field effects, primarily present at the HDA entry and exit, were not taken into account. However, for HDAs used with large PSDs, fringing field effects become important, resulting in departures from the spectrograph properties predicted for ideal fields theoretically.

All studies to date, have basically treated the specific case of a hemispherical spectrometer constructed with the entry and exit apertures placed at the mean radius of the analyser opening (i.e. for radii  $R_1$  and  $R_2$  the entry  $R_0$  is placed at the position  $R_0 = \bar{R} = \frac{R_1+R_2}{2}$ ). In all these cases the potential value  $V_0$  for the circular equipotential line is set to be zero, while the orbit followed by the particles inside the HDA is circular. Analysers whose exit due to geometry limitations could not be placed at  $\bar{R}$  have recently been reported in the literature [9].

In this work the more general case of an HDA in use with a large PSD with paracentric entry (i.e.  $R_0 \neq \bar{R}$ ) and non-zero ( $V_0 \neq 0$ ) entry potential value is studied in detail. The paracentric entry and non-zero entry potential value are considered as free parameters which can be varied, in order to investigate the general focusing and dispersive properties of the HDA.

### Motion of a charged particle in an ideal $1/r$ potential

The HDA model under study is shown in Fig. 5. The analyser consists of two concentric hemispherical plates of inner and outer radii of  $R_1$  and  $R_2$  respectively. The center of the hemispheres is set at the origin of the coordinate system. A paracentric entry is located at distance  $R_0$ , while a PSD is placed at the HDA exit centered at distance  $R_\pi \equiv \bar{R} = \frac{R_1+R_2}{2}$ . A cylindrical lens is mounted with its optical axis centered at the paracentric entry for focusing and deceleration purposes. A particle of charge  $q$  and mass  $m$  and kinetic

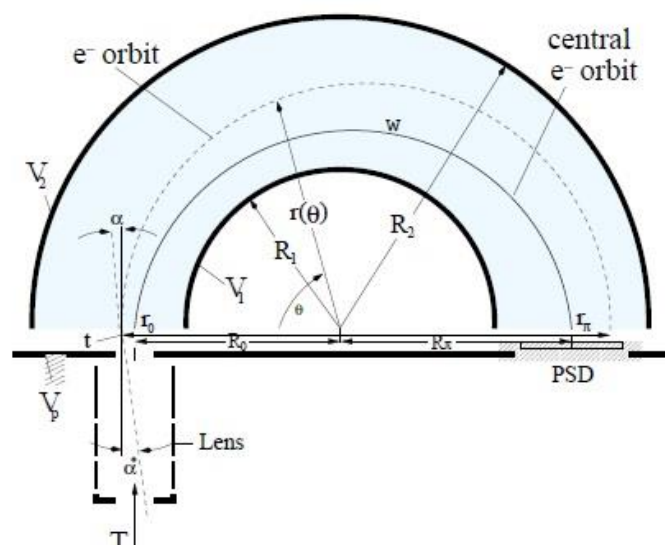


Fig. 5 Schematic diagram of the Hemispherical Deflector Analyser geometry.

energy  $T$  is ejected at zero potential far from the spectrograph. Prior to entering the analyser it passes through a deceleration/focusing stage (e.g. lens system) which can take its kinetic energy to  $t$  such that:

$$t = T - qV_p$$

by applying a potential  $V_p$  on the last electrode of the deceleration stage. When deceleration is not required,  $V_p$  is set to zero ( $V_p = 0$ ). However, when deceleration is used  $V_p$  is the voltage upon which all analyser potentials are referenced to.

The particle enters the HDA at a point  $r_0$  (in the vicinity of  $R_0$ ) with kinetic energy  $t$  and polar angle  $\alpha$ . Actually, since the particle is ejected in three-dimensional space, it enters the analyser at an azimuthal angle  $\beta$  too. However,  $\beta$  just rotates the motion plane around the axis defined by the entrance point  $r_0$  and the center of the analyser. This is the reason why it is not included in the figure which shows the motion in the orbit plane only. The particle follows a trajectory specified by  $r(\theta)$  and exits at  $r_\pi$  after being deflected through an angle  $\Delta\theta = \pi$ .

The analyser potential  $V(r)$  is ideally given by  $V(r) = \tilde{V}(r) + V_p$  where the symbol  $\tilde{V}(r)$  is used as a shorthand for the frequently appearing quantity:

$$\tilde{V}(r) = -\frac{k}{r} + c$$

The symbols  $V_1 \equiv V(R_1)$ ,  $V_2 \equiv V(R_2)$  and the corresponding  $\tilde{V}_1, \tilde{V}_2$  are reserved for the inner and outer hemispheres, respectively. Also, the symbol  $V_0 \equiv V(R_0)$  and the corresponding  $\tilde{V}_0$  is reserved for the value of the potential at the entry  $R_0$ . Finally the quantities  $\Delta V \equiv V_2 - V_1 = \tilde{V}_2 - \tilde{V}_1$  and  $\Delta R \equiv R_2 - R_1$  are defined.

When the analyser is “tuned” to the energy  $w$ , an electron with kinetic energy  $t = w$  can be made to follow a particular reference trajectory known as the *central trajectory*, in which case the particle is also referred to as the central ray and  $w$  as the tuning energy.

For analyzing systems with deceleration, as in the present system, one may define an “undecelerated tuning energy”  $W$ :

$$W \equiv w + qV_p$$

and the deceleration ratio  $F$ :

$$F \equiv \frac{W}{w}$$

so that a central ray with kinetic energy  $W$  far from the spectrometer (at “infinity”) undergoing deceleration with factor  $F$  will have the energy  $w$  just prior to entering the hemispherical analyser. The “reduced” pass energy  $\tau$  is also defined as:

$$\tau \equiv \frac{t}{w} = F \left( \frac{T}{W} - 1 \right) + 1$$

which may also be expressed in terms of the undecelerated quantities,  $T$ ,  $W$  and the deceleration factor  $F$ . Finally, the independent parameter  $\gamma$  by which the potential set on the analyser is controlled:

$$q(V_0 - V_p) = q\tilde{V}_0 \equiv (1 - \gamma)w$$

and the parameter  $\xi$ , characterizing the 'asymmetry' of the HDA:

$$\xi \equiv \frac{R_\pi}{R_0}$$

The parameter  $\gamma$  is known as the entry bias parameter. A conventional HDA is seen to have  $\xi = 1$  and  $\gamma = 1$ .

## Derivation of a charged particle trajectory

The motion of a charged particle of mass  $m$  and charge  $q$  in a central potential  $V(r)$  is always motion in a plane. The problem is equivalent to the "two body" problem, the general solution of which can be found in most undergraduate textbooks of classical mechanics.

The solution of the orbital motion will be derived in brief steps taking the fixed center of force which corresponds to the potential as the origin of the coordinate system.

Expressed in plane polar coordinates the Lagrangian is:

$$\mathcal{L} = \frac{1}{2}m(\dot{r}^2 + r^2\dot{\theta}^2) - qV(r)$$

The Euler-Lagrange equations of motion are:

$$\begin{aligned} \frac{d}{dt} \left( \frac{\partial \mathcal{L}}{\partial \dot{\theta}} \right) - \frac{\partial \mathcal{L}}{\partial \theta} &= 0 \Rightarrow \frac{d}{dt} (mr^2\dot{\theta}) = 0 \\ \frac{d}{dt} \left( \frac{\partial \mathcal{L}}{\partial \dot{r}} \right) - \frac{\partial \mathcal{L}}{\partial r} &= 0 \Rightarrow m\ddot{r} - mr\dot{\theta}^2 = -q \frac{\partial V(r)}{\partial r} \end{aligned}$$

Integrating the equations of motion the first integrals of motion are obtained:

$$\begin{aligned} \Rightarrow mr^2\dot{\theta} &= \text{const.} = L \\ \Rightarrow \frac{1}{2}m\dot{r}^2 + \frac{1}{2} \frac{L^2}{mr^2} + qV(r) &= E \end{aligned}$$

$L$  is the magnitude of the angular momentum of the system while  $E$  is the total energy. Two more integrations are needed to solve the equations of motion, since there are two variables,  $r$  and  $\theta$ . After two more integrations the above equations give

$$\theta = \int_{r_0}^r \frac{dr}{r^2 \sqrt{\frac{2mE}{L^2} - \frac{2mqV(r)}{L^2} - \frac{1}{r^2}}} + \theta_\varepsilon$$

where  $r_0$  and  $\theta_\varepsilon$  are defined by the initial conditions. This is the most general solution of the equation of motion. Replacing the general central potential  $V(r)$  with the electrostatic

potential of a spherical capacitor, the final solution of the particle orbit inside a spherical analyser is obtained

$$r(\theta) = \frac{\frac{L^2}{mqk}}{1 + \sqrt{1 + \left(\frac{2E'L^2}{mqk^2}\right) \cos(\theta - \theta_\varepsilon)}} = \frac{p}{1 + \varepsilon \cos(\theta - \theta_\varepsilon)}$$

The above equation is the general solution of a conic section with one focus at the origin and latus rectum  $p$  and eccentricity  $\varepsilon$  given by the equations:

$$p = \frac{L^2}{mqk}$$

$$\varepsilon = \sqrt{1 + \frac{2E'L^2}{mqk^2}}$$

$E'$  is a quantity with dimensions of energy which defines the nature of the orbit by defining the magnitude of  $\varepsilon$  and is defined as

$$\frac{1}{2}mr\dot{\theta}^2 + \frac{1}{2}\frac{L^2}{mr^2} - q\frac{k}{r} = E - qc - qV_p \equiv E'$$

In the case of the elliptical orbit –which is the case of a charged particle orbit inside the spherical analyser- the equation of the article orbit is reduced to

$$r(\theta) = \frac{a(1 - \varepsilon^2)}{1 + \varepsilon \cos(\theta - \theta_\varepsilon)}$$

where  $a$  is the semi-major axis given by:

$$a = -\frac{qk}{2E'}$$

## Focusing Conditions of the Ideal HDA

The focusing conditions of the ideal hemispherical analyser are directly obtained by expanding the elliptical orbit equation to second order in  $a$  around  $a = 0$ .

$$\frac{r_0}{r_\theta} = \frac{qk + (2tr_0 - qk)\cos\theta}{2tr_0} - (\sin\theta)\alpha + \frac{qk(1 - \cos\theta)}{2tr_0}a^2$$

The first order term in  $a$  is readily seen to be zero for  $\theta = \pi$  and thus the hemispherical deflector analyser (HDA) is said to focus to first order for a deflection angle of  $180^\circ$ . Particles that enter the HDA with the same radius  $r = r_0$  and the same energy but different angles  $\alpha$ , after a deflection of  $180^\circ$ , will all lie on radii  $r_\pi = r(\theta = \pi, \alpha)$ , which will only differ to second order in  $\alpha$ . The most important feature of the HDA is its all order focusing at  $\theta = \pi$  for the azimuthal angle  $\beta$ .

## Spectrograph basic equation

Since the HDA focusing properties can be studied only from the ray trace on the exit plane, an expression which gives the position of the particle at the image (exit), as a function of its position and direction at the object (entrance) and its pass energy  $\tau$  can be derived:

$$r_{\pi} = -r_0 + \frac{R_0(1 + \xi)}{1 + \frac{\xi}{\gamma}(1 - \tau \cos^2 a^*)}$$

This kind of equation is known as the basic equation of the spectrograph. The equation can also be written (in terms of potential constants  $k$  and  $c$ ) in the form

$$r_{\pi} = -r_0 + \frac{qk}{qc - t \cos^2 a^*}$$

or may be rearranged into the usual form:

$$\frac{r_{\pi} - R_{\pi}}{R_{\pi}} = -\frac{(r_0 - R_0)}{\xi R_0} - \left(1 + \frac{1}{\xi}\right) \frac{1}{1 + \frac{\xi}{\gamma} \sin^2 a^* - (\tau - 1) \frac{\xi}{\gamma} (1 - \sin^2 a^*)}$$

The first of the three equations shows that the range of the electron trajectory inside the analyser (i.e. the sum  $r_{\pi} + r_0$ ) is a universal function of the "reduced" pass-energy  $\tau$  and the incident angle  $\alpha$ . This, universal scaling with  $\tau$  is particularly useful during the energy calibration of the spectrometer since different energies  $T$  and deceleration factors  $F$  must all fall on one universal curve dependent on  $\tau$ , avoiding the tedious task of calibrating the spectrometer for all combinations of  $F$ ,  $T$  and  $W$  used.

## Analyzer Voltages

The voltage scheme  $V_1$  and  $V_2$  applied on the inner and outer spherical shells of the analyser, respectively, is actually a function of the tuning energy of the spectrometer.

The determination of the voltages is based on the concept of "central" ray, in a straightforward way. The entry and exit points are specified. For these points, a central or reference ray with  $a = 0$  and pass energy  $t$ , set to the analyser tuning energy  $w$ , i.e.  $t = w$ , is decided. These conditions are adequate to define the proper potential applied on the analyser. In this study, the central ray is defined such that a charged particle enters at  $r = R_0$  (i. e.  $r_0 = R_0$ ) and exits after a deflection by  $180^\circ$  at  $r = \bar{R} \equiv (R_1 + R_2)/2$ .

Applying voltages  $V_1$  and  $V_2$  on the inner and outer spherical shells of the analyser, respectively, the expressions for  $k$  and  $c$  are obtained:

$$c = \frac{R_2 V_2 - R_1 V_1}{\Delta R} - V_p = \frac{R_2 \bar{V}_2 - R_1 \bar{V}_1}{\Delta R}$$

$$k = \frac{\Delta V}{\Delta R} R_1 R_2 = \frac{\Delta \tilde{V}}{\Delta R} R_1 R_2$$

Substituting  $k$  and  $c$  from the expressions above into the spectrograph basic equation, the central ray case reduces to:

$$R_\pi = -R_0 - \frac{q\Delta V R_1 R_2}{q\tilde{V}_1 R_1 - q\tilde{V}_2 + w\Delta R}$$

Furthermore, for a pre-specified entrance potential  $V_0$ , after substitution of  $k$  and  $c$  in terms of  $V_1$  and  $V_2$ ,  $V_0$  is written in terms of  $V_1$  and  $V_2$ :

$$V_0 = \frac{(R_2 - R_0)R_1 V_1 + (R_0 - R_1)R_2 V_2}{\Delta R R_0}$$

And

$$\tilde{V}_0 = \frac{(R_2 - R_0)R_1 \tilde{V}_1 + (R_0 - R_1)R_2 \tilde{V}_2}{\Delta R R_0} + V_p$$

Finally, solving for  $V_1$  and  $V_2$  the voltage equations are obtained:

$$qV_i = qV_p + w + [q(V_0 - V_p) - w] \frac{R_0(R_\pi + R_0 - R_i)}{R_\pi R_i} \quad i = 1,2$$

Or expressed in terms of the  $\tilde{V}$  potentials:

$$q\tilde{V}_i = w + (q\tilde{V}_0 - w) \frac{R_0(R_\pi + R_0 - R_i)}{R_\pi R_i} \quad i = 1,2$$

Which uniquely determine  $V_1$  and  $V_2$  in terms of potentials  $V_0, V_p$ , the tuning energy  $w$  and the "central ray" positions of the entrance  $R_0$  and the exit  $R_\pi$ , respectively. This is the most general formula for the voltages from which all specific cases can be derived.

The potential energy difference  $q\Delta V$  is:

$$q\Delta V = \left(\frac{\gamma}{\xi}\right) \frac{(1+\xi) R_\pi \Delta R}{R_1 R_2} w$$

From which a spectrometer constant  $f$  can be defined to be:

$$f \equiv q \frac{\Delta V}{w} = \frac{1}{2} \left(\frac{\gamma}{\xi}\right) \frac{(1+\xi) R_\pi}{\bar{R}} f_0$$

Where  $f_0$  is just the spectrometer constant of the conventional hemispherical analyser, i.e.  $R_0 = \bar{R} = R_\pi$  with  $V_0 = V_p$  ( $\gamma = 1$ ):

$$f_0 = \frac{\Delta R}{R_2 R_1} 2\bar{R}$$

The constant of the analyser  $f$  is actually a number which determines the gradient voltage value applied on the plates, for tuning the spectrometer at a given energy  $t = w$ . This number was introduced in the past for convenience, since in most spectrometers it uniquely defines the voltages set on the analyser as a function of  $w$ . However, in the paracentric HDA case,  $f$  does not determine the voltage values  $V_1$  and  $V_2$  uniquely, since the information on  $V_0$  (or  $\gamma$ ) value is also needed. Therefore  $f$  is only a qualitative number describing the actual potential gradient between the hemispheres.

For further details on the theory behind the HDA and how these equations derive analytically the reader is referenced to the following citations [10] [11] [12].

## Ion Optics Simulation Software SIMION

SIMION is a very powerful user-friendly ion-optics package that can simulate the trajectories of charged particles flying in a setup consisting of electrostatic and/or magnetostatic elements. In SIMION the space is transformed to a 3-dimensional grid, and the potential at each grid point of the volume is calculated for every element, using a relaxation method. Ions are flying in the 3-dimensional space by experiencing the electrostatic and/or magnetostatic forces of the estimated potential at each grid point. Relativistic are also included in the ion-optics treatment. SIMION provides extensive supporting functionality in geometry definition, user programming, data recording, and visualization. The reader is referred to the SIMION 8.1 website for more information [13].

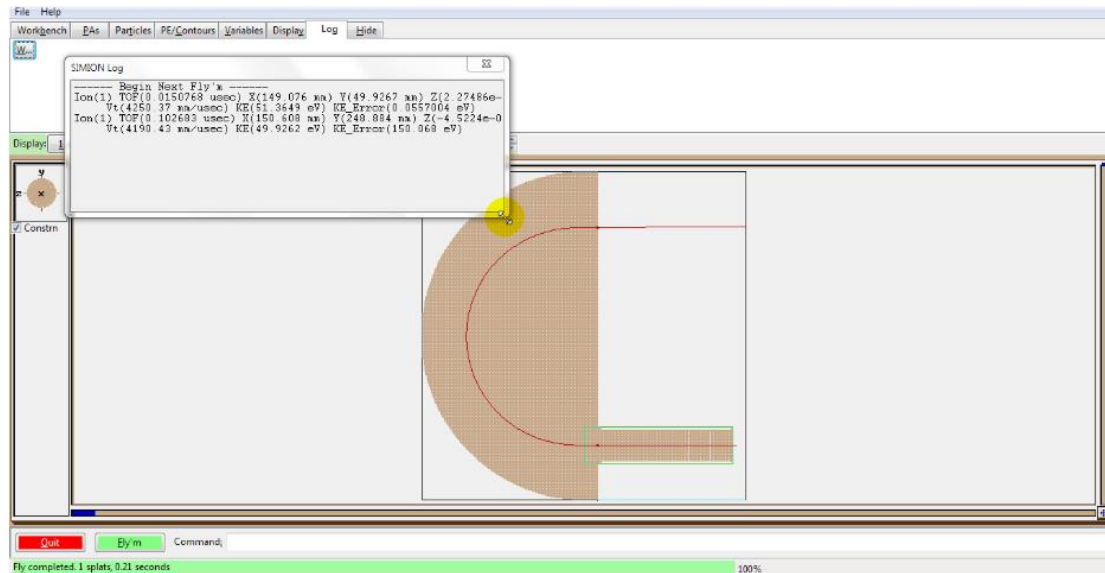


Fig. 6. The main SIMION 8.1 user interface, showing the HDA with lens being simulated during a run with a beam of electrons. On the upper left side the log window can be seen with the results obtained through the data recording feature.

## References

- [1] H. Hertz, "Ueber den Einfluss des ultravioletten Lichtes auf die electrische Entladung," vol. 267, no. 8, p. 983–1000, 1987.
- [2] A. Einstein, "Über einen die Erzeugung und Verwandlung des Lichtes betreffenden heuristischen Gesichtspunkt (On a Heuristic Point of View about the Creation and Conversion of Light)," *Annalen der Physik*, vol. 17, no. 6, p. 132–148, 1905.
- [3] P. D. Innes, "On the Velocity of the Cathode Particles Emitted by Various Metals under the Influence of Rontgen Rays, and Its Bearing on the Theory of Atomic Disintegration," *The Royal Society*, vol. 79, no. 532, 1907.
- [4] E. Rutherford, "The Scattering of  $\alpha$  and  $\beta$  rays by Matter and the Structure of the Atom," *Philosophical Magazine*, vol. 21, no. 6, pp. 669-688, 1911.
- [5] N. F. Mott and H. W. Massey, *The theory of atomic collisions*, Oxford: Oxford University Press, 1933.
- [6] A. L. Hughes and V. Rojansky, "On the analysis of electrostatic velocities by electrostatic means," vol. 34, 1929.
- [7] E. M. Purcell, "The focusing of charged particles by a spherical condenser," vol. 54, 1938.
- [8] C. E. Kuyatt and J. A. Simpson, "Electron Monochromator Design," vol. 38, no. 1, 1967.
- [9] V. D. B. a. M. I. Yavor, *Rev. Sci. Instrum.*, no. 71, p. 1651, 2000.
- [10] E. P. Benis, "A novel high-efficiency paracentric hemispherical spectrograph for zero-degree auger projectile spectroscopy," Heraklion, 2001.
- [11] E. P. B. a. T. J. M. Zouros, "The hemispherical deflector analyser revisited: II. Electron-optical properties," *J. Electron Spectrosc. Relat. Phenom.*, vol. 163, no. 1-3, pp. 28-39, 2008.
- [12] T. J. M. Z. a. E. P. Benis, *J. Electron Spectrosc. Relat. Phenom*, vol. 142, no. 125, pp. 221-248, 2005.
- [13] "The field and particle trajectory simulator - Industry standard charged particle optics software SIMION," [Online]. Available: [www.simion.com](http://www.simion.com).

## Appendix A (Works Cited)

### Articles in International Journals

Experimental energy resolution of a paracentric hemispherical deflector analyzer for different entry positions and bias, M. Dogan, M. Ulu, G. G. Gennarakis, T.J.M. Zouros, Review of Scientific Instruments **84** (2013) 043105

### Posters Presentations for International Conferences/Meetings

M. Dogan, M. Ulu, G. G. Gennarakis, T.J.M. Zouros, ICPEAC 2013, July 24-30, 2013, Lanzhou, China Poster Contribution

### Posters Presentations for Local Conferences/Meetings

G. G. Gennarakis, T. J. M. Zouros, M. Dogan, M. Ulu, 22nd Hellenic Nuclear Physics Symposium, May 31-June 1, 2013, Athens, Greece Poster Contribution 2

### Abstracts for Local Conference/Meetings

G. G. Gennarakis, T. J. M. Zouros, M. Dogan, M. Ulu, HNPS2013: May 31-June 1, 2013, Athens, Greece

### Articles in Local Proceedings

Experimental energy resolution of a paracentric hemispherical deflector analyzer for different entry positions and bias simulated in SIMION, G.G. Gennarakis, T.J.M. Zouros, 22nd Hellenic Nuclear Physics Symposium, May 31-June 1, 2013, Athens, Greece, Proceedings.

## Appendix B (Research Papers Published)

## Experimental energy resolution of a paracentric hemispherical deflector analyzer for different entry positions and bias

M. Dogan, M. Ulu, G. G. Gennarakis, and T. J. M. Zouros

Citation: *Review of Scientific Instruments* **84**, 043105 (2013); doi: 10.1063/1.4798592

View online: <http://dx.doi.org/10.1063/1.4798592>

View Table of Contents: <http://scitation.aip.org/content/aip/journal/rsi/84/4?ver=pdfcov>

Published by the [AIP Publishing](#)

---

**GRANVILLE-PHILLIPS®**  
ADVANCED VACUUM MEASUREMENT SOLUTIONS

Vacuum Gauges:  
Convectron®, Micro-Ion®, Stabil-Ion®,  
Cold Cathode

Mass Spectrometers:  
Vacuum Quality Monitors

 Brooks [www.brooks.com](http://www.brooks.com)

Introducing the First  
**Cold Cathode Gauge**  
worthy of the  
**Granville-Phillips name!**

- Unsurpassed Accuracy
- Predictive & Easy Maintenance



# Experimental energy resolution of a paracentric hemispherical deflector analyzer for different entry positions and bias

M. Dogan,<sup>1,a)</sup> M. Ulu,<sup>1</sup> G. G. Gennarakis,<sup>2</sup> and T. J. M. Zouros<sup>2</sup>

<sup>1</sup>*eCOL Laboratory, Department of Physics, Science and Arts Faculty, Afyon Kocatepe University, 03200 Afyonkarahisar, Turkey*

<sup>2</sup>*Atomic Collisions and Electron Spectroscopy Laboratory, Department of Physics, University of Crete, P.O. Box 2208, 71003 Heraklion, Crete, Greece*

(Received 6 March 2013; accepted 14 March 2013; published online 10 April 2013)

A specially designed hemispherical deflector analyzer (HDA) with 5-element input lens having a movable entry position  $R_0$  suitable for electron energy analysis in atomic collisions was constructed and tested. The energy resolution of the HDA was experimentally determined for three different entry positions  $R_0 = 84, 100, 112$  mm as a function of the nominal entry potential  $V(R_0)$  under pre-retardation conditions. The resolution for the (conventional) entry at the mean radius  $R_0 = 100$  mm was found to be a factor of 1.6–2 times *worse* than the resolution for the two (paracentric) positions  $R_0 = 84$  and 112 mm at particular values of  $V(R_0)$ . These results provide the first *experimental* verification and a proof of principle of the utility of such a paracentric HDA, while demonstrating its advantages over the conventional HDA: greater dispersion with reduced angular aberrations resulting in better energy resolution without the use of any additional fringing field correction electrodes. Supporting simulations of the entire lens plus HDA spectrometer are also provided and mostly found to be within 20%–30% of experimental values. The paracentric HDA is expected to provide a lower cost and/or more compact alternative to the conventional HDA particularly useful

## I. INTRODUCTION

The hemispherical deflector analyzer (HDA) is one of the most widely used electrostatic energy selectors in low energy atomic collision physics (for a recent review see Ref. 1 and the references therein). However, the first-order focusing characteristics of a HDA are impaired due to the fringing fields created at the electrode entry boundaries. In the conventional HDA, fringing fields generally produce an image with larger angular aberrations at the dispersion plane from that predicted for the ideal (no fringing fields) HDA leading to a substantial deterioration in its energy resolution.<sup>1</sup> Partial recovery of the high resolution attributes of the ideal HDA can be attained by incorporating additional electrodes in various fringing field correction schemes.<sup>2</sup> Over the last decade, it has been shown in simulation<sup>2–5</sup> that this drawback can also be readily overcome without using any type of additional fringing field corrector electrodes in an arrangement that has come to be known as the “biased paracentric” HDA.<sup>5</sup> This HDA utilizes a biased optical axis (i.e., the central ray trajectory is not at 0 potential as in a conventional HDA) and an optimized entry position  $R_0$  *offset* from the center position (at the mean radius  $\bar{R} = (R_1 + R_2)/2$ ) used in conventional HDAs.<sup>5</sup> Previous simulations have shown<sup>2–5</sup> that the biased paracentric HDA can in principle restore near ideal field conditions. To date, however, these expectations have not been tested experimentally since they require a direct comparison of conventional and paracentric entries in the *same* analyzer necessitating a HDA with a *variable* entry radius  $R_0$ . Since HDAs are

typically also equipped with an input lens this would require, in addition, special hardware allowing for the precise repositioning of the entire electron source, lens and entry aperture assembly at the various entry radii to be tested, clearly requiring a special arrangement. In this paper we report on first experimental results using such a variable entry HDA, specifically designed for testing the biased paracentric HDA concept experimentally and the energy resolution improvements claimed by simulation.

The design considerations outlined in our previous simulation work<sup>5</sup> were realized experimentally here and the new biased paracentric HDA configuration for atomic collisions was constructed and tested. The present analyzer uses a wide-gap inter-electrode distance  $l \equiv R_2 - R_1 = 50$  mm and a mean radius  $\bar{R} = 100$  mm. It incorporates a standard input lens, which in this case is mounted on a rail to allow for the repositioning of the entry at any value  $R_0$  between the inner hemisphere at radius  $R_1 = 75$  mm and the outer hemisphere at  $R_2 = 125$  mm. The apparatus is shown in Fig. 1. Here, we report on energy resolution measurements for two paracentric entry positions  $R_0 = 84$  mm and  $R_0 = 112$  mm, on either side of the mean radius, respectively, in comparison to the conventional (central) entry at  $R_0 = \bar{R} = 100$  mm. These specific  $R_0$  entry positions were predicted<sup>5</sup> from our previous simulation work<sup>2,4</sup> to correspond to positions of optimal energy resolution for the right entry bias.

We note that our reported experimental measurements are performed on a combined ESCA-type spectrometer (comprised of a HDA with input lens) under pre-retardation conditions, typical in high resolution electron spectroscopy applications. This necessitated the use of new additional simulations

<sup>a)</sup>Author to whom correspondence should be addressed. Electronic mail: mdogan@aku.edu.tr

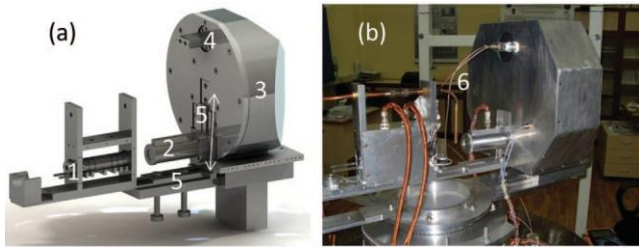


FIG. 1. (a) 3D drawing of the complete analyzer system, showing its five main parts: (1) electron gun, (2) input lens, (3) HDA, (4) detector CEM assembly, and (5) movable supporting rail. The electron gun and input lens are seen to be assembled on the same movable supporting rail. (b) Photograph of the actual setup also showing the vertical gas nozzle jet target (6). Here,

the electron gun is seen to lie across the analyzer while in the measurements

it was used at  $90^\circ$ . The supporting rail can be moved up or down along the direction of the double arrows, effectively changing the entry position of the

under pre-retardation conditions, which are also presented for comparison.

## II. ELECTRON OPTICAL PROPERTIES

The energy dispersing properties and focusing action of the biased paracentric HDA have been discussed in a number of articles.<sup>1-5,7</sup> We therefore present here only a short summary of important relevant characteristics.

The general potential  $V(r)$  in an *ideal* HDA can be obtained<sup>1</sup> from the analysis of the general trajectory equations applied to the *central ray*. This is used as the reference trajectory entering the HDA with *pass energy*  $E_0$  and input angle  $\alpha = 0^\circ$  at the entry radius  $R_0$  and exits after deflection by  $180^\circ$  through the analyzer at the radius  $R_\pi$  here set to be equal to the mean radius, i.e.,  $R_\pi = \bar{R}$ . Thus, the  $V(r)$  potential (referenced to absolute ground) is given by<sup>1</sup>

$$qV(r) = E_0 \left[ F - \gamma \frac{R_0}{R_\pi} \frac{(R_0 + R_\pi)}{r} - 1 \right]. \quad (1)$$

The voltages on the hemispherical electrodes  $V_1 = V(R_1)$  and  $V_2 = V(R_2)$ , as well as at the entry  $V_0 = V(R_0)$ , can then be directly obtained from Eq. (1) for  $r = R_1$ ,  $R_2$  and  $R_0$ , respectively.  $F$  is the pre-retardation ratio  $E_{s0}/E_0$  where  $E_{s0}$  is the electron source energy ( $F = 1$  when no pre-retardation is used). The parameter  $\gamma$ , known as the entry *biasing parameter*,<sup>1,7</sup> is related to the entry bias  $V_0$  through Eq. (1) for  $r = R_0$  giving  $qV_0 = (F - \gamma)E_0$ . Here,  $\gamma$  is used as an *independent* variable needed in the specification of both

hemisphere voltages  $V_i$  and entry bias  $V_0$ .  $\gamma$  can be shown to be equivalent to the relative index of refraction across the lens/HDA interface.<sup>7</sup>

A conventional HDA typically uses symmetrical entry and exit conditions  $R_0 = R_\pi = \bar{R}$  (and therefore is also referred to as a centric HDA). When no pre-retardation is used ( $F = 1$ ), it also has zero bias, i.e.,  $V_0 = 0$  or  $\gamma = 1$ . On the other hand, a biased paracentric HDA uses asymmetric entry and exit conditions, and thus typically has  $R_0 \neq \bar{R}$  and non-zero bias  $V(R_0) \neq 0$  or equivalently  $\gamma \neq 1$ . Thus, a biased paracentric HDA is seen to represent a more general class of

where the central ray is in general part of an ellipse, while in the conventional HDA it is part of a circle.<sup>1</sup>

An electron entering a HDA (tuned to pass a central ray of energy  $E_0$ ), in the vicinity of the entry at  $r_0 = R_0 \pm \prime r_0/2$  with a pass energy  $E \pm \prime E/2$  and small input half-angle  $\alpha$ , will exit the HDA (after  $180^\circ$  deflection) at the radius  $r_\pi = R_\pi \pm \prime r_\pi/2$ . Under these conditions, the exit beam width along the energy dispersion direction,  $\prime r_\pi$ , is given to 2nd order in  $\alpha$  by<sup>10</sup>

$$\prime r_\pi = |M| \prime r_0 + D_\gamma \frac{\prime E}{E} + P_1 \alpha + P_2 \alpha^2. \quad (2)$$

Here,  $M$  is the linear magnification,  $D_\gamma$  is the  $\gamma$ -dependent dispersion length  $D_\gamma \equiv E \partial r_\pi / \partial E$ , while  $P_1$  and  $P_2$ , are the first- and second-order angular aberration coefficients, respectively. This formula has also been used to parameterize the *real* fringing field HDA by determining the coefficients  $M$ ,  $D_\gamma$ ,  $P_1$ , and  $P_2$ , taking into account the distribution of the electrons over the entry radius  $r$  and half-angle  $\alpha$ . These were obtained<sup>2</sup> as least square fitting parameters for various HDA fringing field corrections schemes. In the case of the *ideal* HDA we have  $M = -1$ ,  $P_1 = 0$ , and  $P_2 = -D_\gamma$ , where  $D_\gamma$  is given by<sup>7</sup>

$$D_\gamma = \frac{R_\pi + R_0}{\gamma} \frac{R_\pi}{R_0}. \quad (3)$$

$P_1 = 0$  means that the ideal HDA has first-order focusing.

For a *monoenergetic* ( $\prime E = 0$ ) beam of electrons going through a HDA with voltages  $V_i$  set to pass the central ray

of energy  $E_0$ , it can be readily shown<sup>7-10</sup> from Eq. (2) that the HDA *base* energy resolution  $R_{B0}$  is related to the *maximal* beam width  $\prime r_{\pi \max}$  by

$$R_{B0} \equiv \frac{\prime E_B}{E_0} = \frac{\prime r_{\pi \max} + w_2}{D_\gamma}, \quad (4)$$

where  $w_2$  is the HDA exit slit width along the dispersion direction. In the case where a PSD is used instead of an exit slit,  $w_2$  is near zero. Both  $\prime r_{\pi \max}$  and  $D_\gamma$  can be readily determined from electron trajectory simulations (without the need to separately obtain the  $M$ ,  $P_1$ , and  $P_2$  coefficients) thus making the right side of Eq. (4) very convenient for the direct evaluation of the HDA resolution in simulations as done here. The left side of Eq. (4) is typically used for the experimental determination of the spectrometer base resolution, usually taking  $\prime E_B \approx 2 \prime E_{\text{FWHM}}$ , the energy resolution at the full width half maximum (FWHM), as also done here.

For the ideal HDA, assuming uniform entry illumination,  $\prime r_0$  in Eq. (2) can be replaced by the entry slit width  $w_1$  and the *base* energy resolution is then given by the well-known formula

$$R_{B0 \text{ ideal}} = \frac{\prime E_B}{E_0} = \frac{w_1 + w_2}{r} + \alpha_{\max}^2 \quad (\text{Ideal HDA}), \quad (5)$$

where  $\alpha_{\max}$  is the maximum input half-angle in the plane of the dispersion. For the ideal *centric* HDA (i.e., the conventional HDA with  $R_0 = R_\pi$  and  $\gamma = 1$ ), Eq. (3) gives  $D_\gamma = 2R_0$  and thus Eq. (5) leads to the well-known ideal conventional HDA base energy resolution formula.

In most high resolution applications *pre-retardation* is typically used to improve the energy resolution of the HDA

by decelerating the electron beam prior to HDA (lens) entry. This is accomplished by negatively biasing the last input lens element at the potential  $V_{5a} = -(E_{s0} - E_0)$  (the same potential used on the base plate of the HDA). In this case the *overall* base resolution of the HDA is improved by the pre-retardation factor  $F$  and simply given by

$$R_{Bs0} = \frac{f' E_B}{E_{s0}} = \frac{1}{F} \left( \frac{f' E_B}{E_0} \right) \quad (\text{Overall base resolution}). \quad (6)$$

Here  $E_{s0}$  is the original central trajectory electron source energy prior to retardation.

In the case of pre-retardation the value of  $\alpha_{\max}$ , the size of the lens image  $f'r_0$  and  $F$  are all linked via the Helmholtz-Lagrange law and an optimal solution exists given by<sup>11</sup>

$$R_{Bs0 \text{ optimal}} = \frac{f' E_B}{E_{s0}} = \frac{3}{2^{2/3}} \left( \frac{d_p d_s}{2lFD_Y} \right)^{2/3} + \frac{w_2}{FD_Y} \quad (\text{Optimal overall ideal base resolution}), \quad (7)$$

where  $d_p$  is the diameter of the pupil (lens entry aperture),  $d_s$  is the source diameter (height of object), and  $l$  is the distance between source and entry pupil. The optimal resolution  $R_{Bs0 \text{ optimal}}$  should be best seen as the absolute resolution limit of an ideal HDA using an input lens for focusing and pre-retardation and in practice is rarely, if ever, attained. In addition, the actual resolution will also be modified<sup>12</sup> by the distance  $h$  between HDA exit plane and the detection or exit slit plane. When a PSD is used,  $h$  is typically 12–15 mm and can therefore additionally contribute to the resolution. In our present slit setup,  $h \approx 5$  mm and its effect was found to be small and therefore has not been included. In Table I, we list the values of the important parameters.

TABLE I. List of most important geometric parameters used in both experimental setup and theoretical modeling (SIMION simulations and ideal field theoretical calculations).

| Parameter | Values          | Explanation                               |
|-----------|-----------------|---|
| $R_0$     | 84, 100, 112 mm | HDA entry radius                          |
| $R_1$     |                 | HDA inner radius                          |
| $R_2$     | 75 mm           | HDA outer radius                          |
| $w_1$     | 125 mm          | HDA diameter of entry aperture            |
| $w_2$     | 2 mm            | HDA diameter of exit aperture             |
| $h$       |                 |   |
| $s$       | 2 mm            | Gap between HDA plane and exit slit plane |
| $g$       |                 | Length of 5-element cylindrical lens      |
| $d$       | 5 mm            |   |
| $d_p$     | 140 mm          | Lens inter-electrode gap                  |
| $l$       |                 | Lens internal diameter                    |
| $d_s$     | 2.5 mm          | Diameter of pupil (lens entry aperture)   |
|           | 20 mm           |   |
| $E_{s0}$  | 2 mm            | Distance between target and lens          |
| $E_0$     | 50 mm           | Source diameter                           |
| $F$       | 2 mm            | Nominal electron gun energy               |

### III. EXPERIMENTAL SETUP

The spectrometer setup<sup>13</sup> used to test our analyzer is based on the crossed-beams principle and basically consists of a high intensity electron gun, a gas beam target, and the HDA. A near-monoenergetic beam of electrons produced by an e-gun was focused onto the target beam and collected in a Faraday cup, while the scattered electrons were detected as a function of their kinetic energy and the angle through which they were scattered.

A 3D drawing and photograph of the complete analyzer system is shown in Fig. 1(a) and Fig. 1(b), respectively. A mounting plate supported the input lens, hemispheres, and detector. The input lens was mounted on a rail, electrically isolated from the shielding electrode. A screw was used to position the lens system, which could be moved up and down along the dispersion direction thus allowing the entry distance  $R_0$  to be effectively varied. The electron gun was also mounted on the same rail and therefore both e-gun and lens remained aligned on the lens axis as they were both moved up or down together.

A circular (2 mm diameter) lens entrance aperture was used and positioned 50 mm from the scattering center. The analyzer entrance and exit apertures were also circular with a 2 mm diameter. The electron gun could be rotated relative to the analyzer about the axis of the gas jet target. All analyzer parts were made from dural. All surfaces exposed to electrons were covered with soot and all aperture plates were made from molybdenum. The vacuum chamber was pumped by a 500 l/s turbomolecular pump. The background pressure in the vacuum chamber was better than  $8 \times 10^{-8}$  mbar. The chamber was magnetically shielded by both  $\mu$ -metal, which lined the inner wall, and an external Helmholtz coil system. The magnetic fields across the electron beam directions were consequently reduced to a few mG.

A 140 mm long five-element cylindrical electrostatic input lens<sup>13–15</sup> transported the scattered electrons to the analyzer. The electrons were then energy analyzed by the hemispherical deflector and detected by a single channel electron multiplier (CEM). The electronic circuits (voltage supply and signal processing) needed for the operation of the analyzer is shown in Fig. 2. All the potentials for the input lens and the deflector electrodes, namely  $V_{1a-5a}$ ,  $V_1$ , and  $V_2$ , could be independently tuned by a set of potentiometers with low ripple HV power supplies. The signal from the CEM was amplified by a fast amplifier (Philips Scientific 777) and discriminated by a constant fraction discriminator (Philips Scientific 705). By scanning the deceleration voltage ( $V_{5a}$ ) and HDA voltages  $V_i$ , the scattered electron profile was transmitted through the analyzer while the pass energy  $E_0 = E_{s0} - e|V_{5a}|$  remained fixed. The voltage ramp applied to  $V_{5a}$  was generated by an Ortec MCS-PCI card and the transmitted beam profile stored in the computer and displayed. The ramp voltage sequence was repeated until a pre-determined statistical accuracy of the signal was obtained. The electron gun was placed at two different positions. In the first position, used to study transmission as a function of  $\gamma$ , the analyzer was located directly across from the electron gun ( $0^\circ$ ) with the CEM used as a Faraday cup. In these tests the value of  $\gamma$  was varied while the electron current

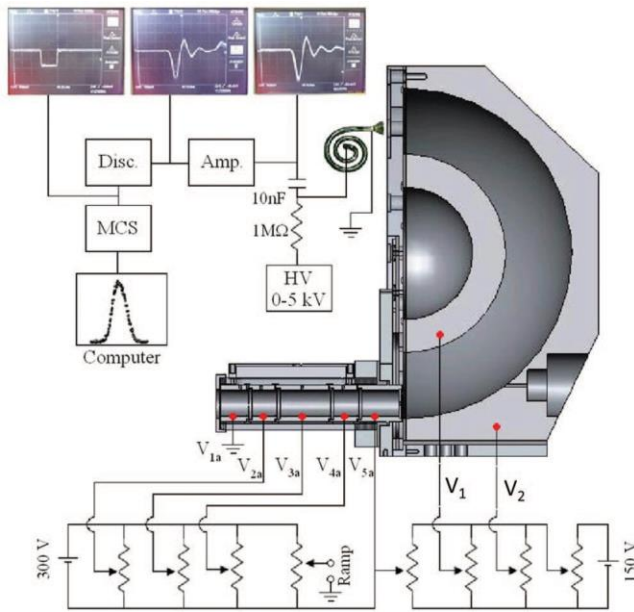


FIG. 2. Analyzer circuit used to operate the analyzer.  $V_{5a}$  is used to retard the electrons down to the pass energy  $E_0$  which was kept fixed during spectrum scans.

passing through the analyzer exit slit was recorded by the current collected in the CEM and measured with a Keithley picoammeter. In the second position, used to determine the energy resolution of the analyzer as a function of  $\gamma$ , the elastic scattering peak was measured for electron-Helium collisions. To measure the elastic energy distribution of the scattered electrons both the electron gun position as well as the angle of the analyzer could be varied. In both positions, the analyzer voltages  $V_1$  and  $V_2$  were set according to Eq. (1) for each of the values of  $\gamma$  and  $R_0$  used. In Sec. IV our  $\gamma$ -dependent results are shown for those electrons that were elastically scattered through  $90^\circ$  before entering the spectrometer. At this scattering angle, spectroscopy results were more detailed and accurate and compared well with the more coarse current measurements of the first position.

## IV. RESULTS

### A. Experiment

The performance of the analyzer was tested by energy analyzing the elastic electron scattering peak for different  $\gamma$  values of the entry bias at the three entry positions,  $R_0 = 100$  mm, 84 mm, and 112 mm, respectively. From the recorded electron line shape the effective resolution of the analyzer was directly determined. In all measurements described here the energy of the electrons emitted from the electron gun was set to  $E_{s0} = 200$  eV. Measurements were then carried out to obtain the peak structure of electrons for pass energies  $E_0 = 30, 40, 50, 60$  eV. In Fig. 3 are shown typical line shapes obtained for the pass energy of  $E_0 = 50$  eV at the fixed scattering angle of  $90^\circ$  with respect to the incident beam, demonstrating the near Gaussian shape of the experimental points. The width of the peaks was determined by the temperature of the filament of the electron gun and the analyzer param-

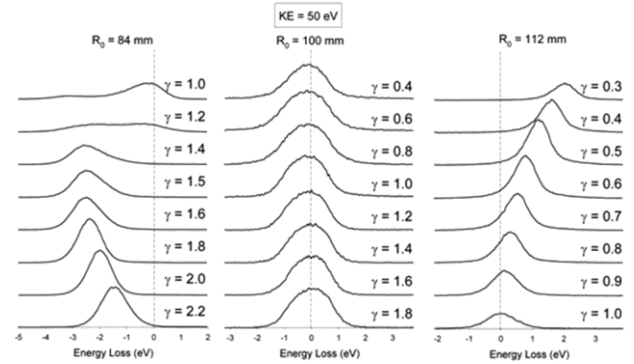


FIG. 3. Electron kinetic energy spectra showing the elastic scattering peak from 200 eV electrons incident on a Helium target for  $R_0 = 84$  mm (left),  $R_0 = 100$  mm (middle), and  $R_0 = 112$  mm (right). The spectrometer was set to

ters. A base energy width of  $\Delta E_{s0} = 0.6$  eV was associated with the gun as determined experimentally. The base energy resolution of the analyzer  $\Delta E_B = \Delta E_{anal}$  was then extracted after deconvolution of the gun resolution, using the relation  $\Delta E_{anal} = \sqrt{\Delta E_{obs}^2 - \Delta E_0^2}$ , where  $\Delta E_{obs}$  is the base width of the observed line shape. The determined overall resolutions for a pass energy of  $E_0 = 50$  eV for the three values of  $R_0$  are shown in Fig. 4 as a function of  $\gamma$ .

### B. SIMION simulations

SIMION simulations are based on the finite difference approach whose accuracy relating to HDAs has been investigated in a previous publication<sup>16</sup> based on the 2005 SIMION 7.0 version. Here, we use the latest 2012 SIMION 8.1 version<sup>6</sup> that has been substantially improved in speed, accuracy, and programming capabilities through the use of many new features such as “surface enhancement” to improve the modeling of curved electrodes, menu driven definitions of initial electron conditions, as well as taking advantage of multi-core, 64-bit PC technology and larger RAM availability.

These technological and software improvements have allowed us to readily simulate the combined HDA plus 5-element input lens in a *single* large 3D potential array (known as an instance in SIMION) using a fairly small fixed density grid size of 0.5 mm per grid unit for an apparatus covering a near cubic volume of more than 300 mm extent on each side. The strong fringing fields between the HDA support plate and the hemispherical electrodes necessitated such a one-instance approach since the image of the lens lies in the fringing field volume. Reflection symmetry in the plane of the dispersion ( $Y = 0$  plane) was used to cut down on RAM. The details of the full 3D trajectory simulations will be described in a forthcoming publication.<sup>19</sup> Here we only give a brief report about our approach as it relates to the evaluation of the energy resolution requiring only a 2D trajectory approach in the plane of the dispersion.

Two different simulation approaches were used in which the same 2D monoenergetic angular electron distribution (saved as a SIMION.ion file) was used for consistency. This

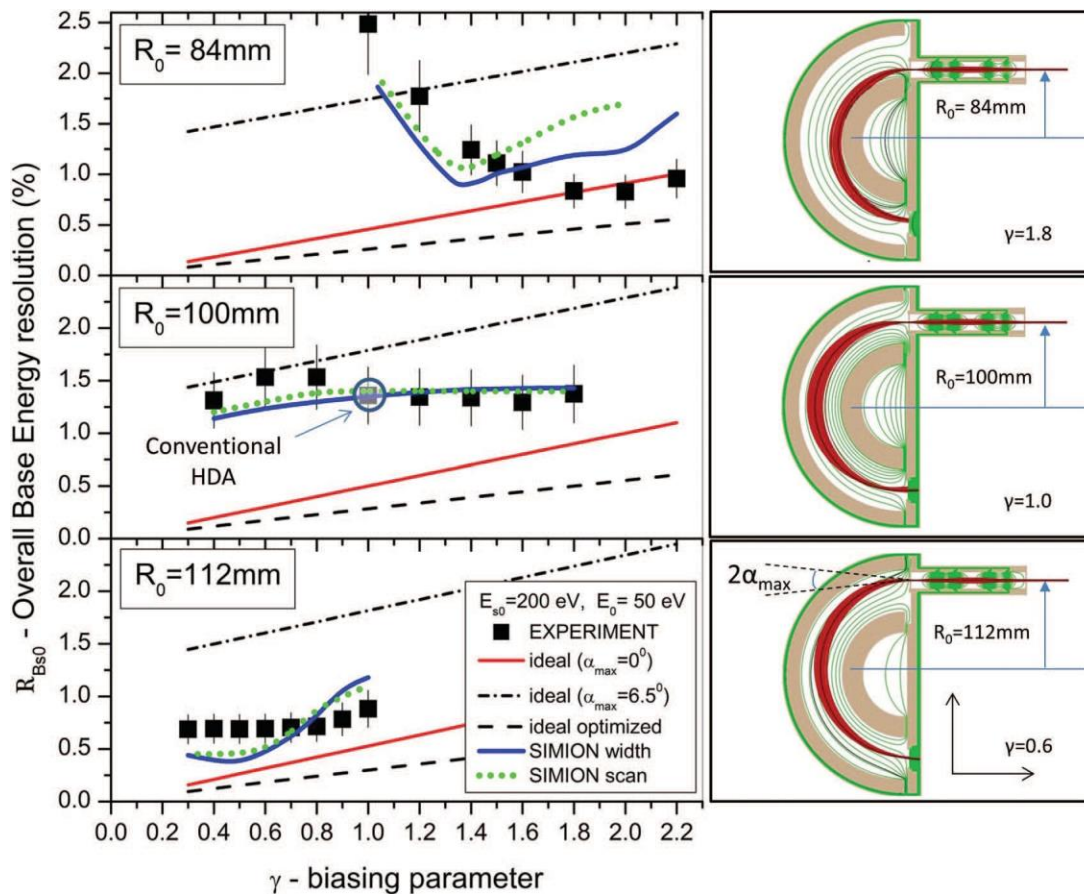


FIG. 4. (Left) HDA overall base energy resolution  $R_{Bs0} = (E_B/E_{s0})$  plotted as a function of the biasing parameter  $\gamma$  for a source energy  $E_{s0} = 200$  eV and pass energy  $E_0 = 50$  eV. Data points: experimental results by spectrum scan for fixed pass energy. Error bars: estimated at  $\pm 20\%$  of  $R_{Bs0}$  to account for possible “mechanical imperfections.”<sup>18</sup> Straight lines: theoretical calculations for an ideal HDA: (full) based on Eq. (5) and  $\alpha_{max} = 6.5^\circ$  (black dashed-dotted) and  $0^\circ$

(red). (Dashed lines) Optimal resolution based on Eq. (7). SIMION simulations: (blue line) exit beam width formula based on Eqs. (4) and (6). (Dotted green line) Spectrum scan for fixed pass energy as in actual measurements. The parameters listed in Table I were used in the formulas and simulations. The conventional HDA entry is marked by a circle at  $R_0 = 100$  mm and  $\gamma = 1.0$  for clear reference. (Right) Schematic of SIMION simulations in the  $Y = 0$  dispersion plane of

distribution represented 10 000 electrons of initial kinetic energy  $E_{s0} = 200$  eV ejected from a source point S with coordinates  $(x_s, y_s = 0, z_s = l = +50$  mm) and passing through a pupil point P with coordinates  $(x_p, y_p = 0, z_p = -1$  mm). The values of both  $x_s$  and  $x_p$  positions were independently and randomly generated (easily done by the new extensive particle menu features of SIMION 8.1) to lie within the corresponding source and pupil limits:  $R_0 - d_s/2 \leq x_s \leq R_0 + d_s/2$  and  $R_0 - d_p/2 \leq x_p \leq R_0 + d_p/2$ , thus defining both the initial position and direction of each electron trajectory flown. In our geometry the lens entry aperture (pupil) was set at  $z = 0$  and had a thickness of 1 mm. All electrons were flown in the dispersion plane ( $Y = 0$ ), which was also the reflection symmetry plane of the whole apparatus with the cylindrical lens axis aligned along the negative Z-axis. For each of the three values of  $R_0$  the lens voltages were set and fixed to the optimally chosen experimental voltages based on past experience with the 5-element lens.<sup>15</sup> HDA voltages were set according to Eq. (1) and therefore depended on both  $R_0$  and  $\gamma$ .

The first simulation approach, termed the “beam width” method, was based on evaluating the right side of Eq. (4) by determining the maximal beam width  $(/')r_{\pi max}$  and dispersion  $D_\gamma \cdot (/')r_{\pi max}$  measured the maximum beam width along the

dispersion direction (x-axis) on the plane of the exit aperture.  $D_\gamma$  was evaluated for each  $\gamma$  by “flying” a set of different energy  $E_i$  trajectories with  $\alpha = 0$  and recording their exit positions  $r_\pi(E_i)$ . A least square linear fit of the form  $r_\pi(E_i) = a + b E_i$ , where a and b are the fitting parameters, then led to the value of  $D_\gamma = E_0 b$ . Substituting the obtained  $D_\gamma$  value into Eq. (4) with  $w_2 = 2$  mm and using Eq. (6) for  $F = 4$  gave the overall base energy resolution shown in Fig. 4 as the blue line.

The second approach termed the “voltage scan” method was almost identical to the way the experimental spectrum (line profile) in Fig. 3 was obtained by stepping the voltages of the HDA and recording the number of electron trajectories that go through the exit aperture for each step. During the scanning of the voltages all lens potentials were kept fixed except for  $V_{5a}$  (also the HDA plate potential), which was stepped so as to keep the pass energy fixed at 50 eV. The voltages were stepped in 0.1 or 0.2 eV steps so as to cover the entire electron peak, which typically extended not more than 2 eV on either side of the central energy of 200 eV. At each step the previously mentioned electron distribution was “flown.”

The base energy  $(/')E_B$  of the line profile could be directly determined from the final energy spectrum and was used in

Eq. (6) to compute the overall base resolution. These results are shown in Fig. 4 as the dotted green line. With the exception of the cases of  $R_0 = 84$  mm with  $\gamma > 1.5$  good overall consistency was found between the two approaches which usually differed by less than  $\sim 15\%$  for most points evaluated. The exceptional cases of  $R_0 = 84$  mm differed by more than 30% for reasons as yet unknown (see below).

### C. Theory—ideal field HDA

Even though the ideal HDA resolution formulas are known to be off, mostly due to the entrance fringing field effects, they are still used as an ultimate guideline and/or limit due to their simplicity. Furthermore, most of the high priced HDAs on the market today do utilize some type of fringing field correction scheme<sup>2</sup> which bring the real HDA resolution specs closer to those of the ideal field. In this spirit, we have listed in Fig. 4 three ideal field calculations for comparison.

The three lines correspond to the well-known resolution formula Eq. (5) with the dispersion calculated from Eq. (3). The first term of Eq. (5) is known as the slit term and the second as the aberration term. Two cases are shown for  $\alpha_{\max} = 0^\circ$  and  $\alpha_{\max} = 6.5^\circ$ . The first corresponds to the trajectory of a central ray, while the second to a ray entering at an angle of  $6.5^\circ$  with respect to the perpendicular to the HDA entry plane. The value of  $6.5^\circ$  was found from our simulations to be indicative for most cases. Typically, however, one strives to keep  $\alpha_{\max}$  as small as possible as it leads to asymmetric line shapes with a low energy tail. When pre-retardation is used to improve the overall resolution, larger  $\alpha$  values become inevitable since upon deceleration the electron beam tends to open up, an effect the lens focusing tries to compensate for. For optimal resolution, a compromise is usually sought that can be arrived at via the Helmholtz-Lagrange law<sup>11</sup> leading to the result of Eq. (7) shown in Fig. 4 as the dashed line. For high values of  $F$ , Eq. (7) approaches the Kuyatt-Simpson criterion<sup>11,17</sup> in which the aberration term is restricted to half the value of the slit term to keep the effect of tailing small.

In Table II we summarize our results for the best experimental resolution values.

## V. DISCUSSION

The results presented in Figs. 3 and 4 represent a unique set of resolution data for the three different entry positions of the same HDA allowing a direct intercomparison. The conventional HDA energy resolution (circle in blue at  $R_0 = 100$  mm and  $\gamma = 1$ ) is clearly seen to be worse (larger) than both biased paracentric cases for  $R_0 = 84$  mm and  $R_0 = 112$  mm depending on  $\gamma$ . Best experimental paracentric resolutions are seen to occur for  $R_0 = 84$  mm at  $\gamma = 1.8$  and for  $R_0 = 112$  mm at  $\gamma = 0.6$  (see Table II). For these settings, the experimental paracentric resolution gains are found to be 1.64 and 1.97 over that of the conventional HDA.

Also shown in Fig. 4 are the resolutions obtained from SIMION simulations of the full HDA plus input lens. Agreement with experiment is seen to be within 20%–30% for the cases of  $R_0 = 112$  mm and 100 mm and fairly consistent between the two different simulation approaches. Such an uncertainty is typical of mechanical tolerances in the construction of HDAs.<sup>18</sup> However, for the case of  $R_0 = 84$  mm and  $\gamma > 1.5$  the discrepancy with experiment is much larger than for all other cases and therefore puzzling. While the trend in the experiment seems to be correctly depicted by the simulations, experimental results are consistently higher than simulation for  $\gamma < 1.5$ , but then cross over for  $\gamma > 1.5$  with the simulation now seeming larger. This turnover is also seen to occur for the  $R_0 = 112$  mm case around  $\gamma = 0.8$ . Improving the simulation grid unit (gu) density by a factor of 4 [to 0.125 mm/gu using special techniques<sup>19</sup> to avoid increasing RAM usage (and refine time) by a factor of  $4^3$  when it was already near 1 GB] for some test cases of  $R_0 = 84$  mm showed only negligible differences giving us confidence that the discrepancy is not due to computational errors in the evaluation of the potentials. It should be noted that for both  $R_0 = 84$  and 112 mm and for values of  $\gamma$  larger than the cross over points the electron trajectories increasingly hit the inner (for  $R_0 = 84$  mm) or the outer (for  $R_0 = 112$  mm) electrode of the HDA, thus reducing the overall transmission of the HDA. Thus, in both such cases, increasing discrepancy between simulation and experiment seems to be correlated with increased loss of transmission.

Another source of uncertainty could also arise from the length of the interaction region in the experiment, which was

TABLE II. Overall base energy resolution  $R_{B50}$  results for an electron source energy  $E_{s0} = 200$  eV and pass energy  $E_0 = 50$  eV. Comparison of lowest experimentally determined values to those from SIMION simulations and ideal field HDA theory. Values of parameters from Table I were used. A conservative estimate of 20% of  $R_{B50}$  was assigned to the experimental values to reflect absolute errors due to possible mechanical imperfections (see text). Resolution gain is computed with respect to the experimental resolution of the conventional fringing field HDA ( $R_0 = 100$  mm,  $\gamma = 1$ ). The HDA voltages used were computed

|                            |                                     | Overall base energy resolution $R_{B50} = (V/E_{s0})E_B/E_{s0}$ (%) |                           |             |                      |                        |      |                 |                    |
|----------------------------|-------------------------------------|---|---------------------------|-------------|----------------------|------------------------|------|-----------------|--------------------|
| Entry radius<br>$R_0$ (mm) | Entry potential<br>$V(R_0)$ (Volts) | Ideal field theory  |                           |             | SIMION simulation    |                        |      | Experiment      | Resolution<br>gain |
|                            |                                     | Optimal (Eq. (7))   | $\alpha_{\max}$ (Eq. (5)) |             | Beam width<br>method | Voltage scan<br>method |      |                 |                    |
| $\gamma$                   |                                     |   | $0^\circ$                 | $6.5^\circ$ |                      |                        |      |                 |                    |
| 100                        | 1.0                                 | −150  | 0.284                     | 0.500       | 1.79                 | 1.35                   | 1.40 | $1.36 \pm 0.27$ | 1.00               |
| 84                         | 1.8                                 | −110  | 0.458                     | 0.822       | 2.11                 | 1.22                   | 1.60 | $0.83 \pm 0.17$ | 1.64               |

estimated to be between 1–2 mm, which is imaged by the lens onto the entry of the HDA. In all simulations a line source of  $d_s = 2$  mm length along the X-direction (dispersion direction) was used giving the best agreement with experimental results. In the past, when only the HDA (without the lens) was simulated, our source always lay within the entry slit of the HDA and results depended sensitively on its extent. Large resolution gains of up to 34 were reported<sup>4</sup> for a point source and 4.2 for a 1 mm source, respectively. Here, it is the size of the image of the original object at the collision region as controlled by the lens magnification that lies within the entry slit. While the lens voltages were set according to best working experience with this lens, a full search for the optimal voltages giving the best resolution was not performed. Such a search can be readily carried out in simulation and could yield still further improvements in the ultimate experimental resolution gains of the paracentric HDAs.

## VI. SUMMARY AND CONCLUSION

In this paper we present, for the first time, direct experimental evidence showing the energy resolution of a biased paracentric HDA to be at least a factor of 1.7–2 times better than the resolution of a conventional HDA, in support of predictions based on previous simulation work. This experimental finding is also in agreement with new simulations presented here which for the first time treat the more realistic case of a HDA with input lens under pre-retardation conditions.

The biased paracentric HDA differs from a conventional HDA in two important ways: (a) the HDA entry distance  $R_0$  is paracentric, i.e., either larger or smaller than the mean HDA radius used in a conventional HDA and (b) the two hemispherical electrode voltages are set so that the entry potential  $V(R_0)$  of the HDA is non-zero (biased), as opposed to conventional HDA usage in which this bias is typically zero. For very particular values of  $R_0$  and  $V(R_0)$ , empirically found through simulations, we have shown<sup>2</sup> in the past that substantial improvements in energy resolution can be made, practically restoring first-order focusing conditions without the use of any additional fringing field correction electrodes, as typically done for conventional HDAs.

The above experimental validation was accomplished by a specially designed HDA with a five-element input lens for which the entry position radius  $R_0$  (i.e., the position of the HDA entry aperture) could be readily moved and placed at any position between  $R_1 = 75$  mm and  $R_2 = 125$  mm, the two radii of the HDA. Thus, we experimentally determined the overall base energy resolution of this HDA for entries  $R_0 = 84, 100, 112$  mm presenting results for the case of pre-retardation factor of  $F = 4$  for various values of the bias  $V(R_0)$  allowing for their direct inter-comparison on the same setup.

The measured improvement in energy resolution is particularly remarkable as it is conveniently attained without the use of any type of additional fringing field correction electrodes, but simply by taking advantage of the strong intrinsic lensing properties of the existing HDA fringing fields as determined and optimized by the particular paracentric entry position and bias control. Clearly, the use of fewer electrodes in the paracentric design reduces its operational complexity

and lowers the overall cost of construction and HV power supplies. Improvement in energy resolution also means that paracentric HDAs of smaller size and therefore weight could replace larger conventional HDAs of equal resolution, particularly attractive to outer space instrumentation applications where both size and weight are invaluable. Finally, not having to introduce cumbersome additional correction electrodes that could partly block transmission, especially when used with a position sensitive detector, is clearly a big advantage.

## ACKNOWLEDGMENTS

This work was supported on the Turkish side by the Scientific and Technological Research Council of Turkey (TUBITAK), through Grant Nos. 106T722 and 109T738. On the Greek side this research has been cofinanced by the European Union (European Social Fund—ESF) and Greek national funds through the Operational Program “Education and Lifelong Learning” of the National Strategic Reference Framework (NSRF)—Research Funding Program: THALES. Investing in knowledge society through the European Social Fund (Grant No. MIS 377289). We are also grateful to the Turkish Patent Institute for funding this work (Registration No: 2009 08700). The authors thank Dr. Omer Sise for his contribution to the initial stages of this investigation and Ahmet Deniz for his help with the technical drawings of the variable entry analyzer. Theo Zouros would also like to thank David Manura of SIS for critically reading the manuscript, as well as for his help with various SIMION 8.1 issues and Lua programming and Professor Kai Rossnagel of the University of Kiel for useful conversations. Finally, we thank Professor Genoveva Martínez López for critically reading the manuscript.

<sup>1</sup>T. J. M. Zouros and E. P. Benis, *J. Electron Spectrosc. Relat. Phenom.* **125**, 221–248 (2002); “Erratum,” **142**, 175 (2005).

<sup>2</sup>O. Sise, T. J. M. Zouros, M. Ulu, and M. Dogan, *Meas. Sci. Technol.* **18**, 1853–1858 (2007).

<sup>3</sup>E. P. Benis and T. J. M. Zouros, *Nucl. Instrum. Methods Phys. Res. A* **440**, 462–465 (2000).

<sup>4</sup>T. J. M. Zouros, O. Sise, M. Ulu, and M. Dogan, *Meas. Sci. Technol.* **17**, N81–N86 (2006).

<sup>5</sup>O. Sise, G. Martínez, T. J. M. Zouros, M. Ulu, and M. Dogan, *J. Electron Spectrosc. Relat. Phenom.* **177**, 42–51 (2010); predictions of optimal paracentric conditions were found to lie at  $R_0 = 85$  mm,  $\gamma = 1.435$ , and  $R_0 = 115$  mm,  $\gamma = 0.672$  for a HDA with  $R_1 = 75$  mm and  $R_2 = 125$  mm. Here the constructed HDA has the same electrode radii, but the  $\alpha$  and  $\hat{\alpha}$  the half-angle after refraction. The two are related by  $\hat{\alpha} = \alpha^* / \sqrt{\gamma^2}$  via Snell’s law and/or the Helmholtz-Lagrange theorem.<sup>8–11</sup> Here, to avoid cumbersome notation, we just use the symbol  $\alpha$  for what in Refs. 1 and 7 was symbolized by  $\alpha^*$ .

<sup>8</sup>Volker Schmidt, *Electron Spectrometry of Atoms Using Synchrotron Radiation* (Cambridge University Press, 1997) (see Eq. (4.7a)).

<sup>9</sup>M. Yavor, “Optics of Charged Particle Analyzers: Chapter 6. Electrostatic

- Radiation*, edited by E. E. Koch (North Holland, Amsterdam, 1983), Vol. 1A, Chap. 6, pp. 367–456.
- <sup>11</sup>T. J. M. Zouros and E. P. Benis, *Appl. Phys. Lett.* **86**, 094105 (2005).
- <sup>12</sup>T. J. M. Zouros, E. P. Benis, and I. Chatzakis, *Nucl. Instrum. Methods Phys. Res. B* **235**, 535–539 (2005).
- <sup>13</sup>M. Dogan, M. Ulu, and O. Sise, *J. Electron Spectrosc. Relat. Phenom.* **161**,
- <sup>15</sup>M. Dogan and A. Crowe, *J. Phys. B* **35**, 2773–2781 (2002).
- <sup>16</sup>T. J. M. Zouros, Omer Sise, F. M. Spiegelhalter, and David J. Manura, *Int. J. Mass Spectrom.* **261**, 115–133 (2007).
- <sup>17</sup>C. E. Kuyatt and J. A. Simpson, *Rev. Sci. Instrum.* **38**, 103–111 (1967).
- <sup>18</sup>B. Wannberg, *Nucl. Instrum. Methods Phys. Res. A* **239**, 269–272 (1985).
- <sup>19</sup>G. G. Gennarakis *et al.*, “Energy resolution of a paracentric hemispherical deflector analyzer for different entry positions and bias: Detailed Mea-